Atmospheric rivers in CMIP5 climate ensembles downscaled with a high resolution regional climate model

Matthias Gröger[1], Christian Dieterich[1†], Cyril Dutheil[1], H.E. Markus Meier[1,2], Dmitry V. Sein[3,4],

[1]Department of Physical Oceanography and Instrumentation, Leibniz Institute for Baltic Sea Research Warnemünde, Rostock, 18119, Germany

[2]Research and Development Department, Swedish Meteorological and Hydrological Institute, Norrköping, 601 76, Sweden

[3] Shirshov Institute of Oceanology, Russian Academy of Sciences; Moscow, Russia

[4] Alfred Wegener Institute, Helmholtz Centre for Polar and Marine Research; Bremerhaven, Germany

[†] deceased

Correspondence to: Matthias Gröger (matthias.groeger@io-warnemuende.de)

Abstract

Atmospheric rivers (AR) are important drivers of hazardous precipitation levels and are often associated with intense floods. So far, the response of ARs to climate change in Europe has been investigated using global climate models within the CMIP5 framework. However, the spatial resolution of those models (1–3°) is too coarse for an adequate assessment of local to regional precipitation patterns. Using a regional climate model with 0.22° resolution, we downscaled an ensemble consisting of 1 ERAI hindcast simulation, 9 global historical, and 24 climate scenario simulations following greenhouse gas emission scenarios RCP2.6, RCP4.5, RCP8.5.

The performance of the climate model to simulate AR frequencies and AR induced precipitation was tested against ERA-Interim reanalysis data (ERAI). Overall, we find a good agreement between the downscaled CMIP5 historical simulations and ERAI. However, the downscaled simulations better represented small-scale spatial characteristics. This was most evident over the terrain of the Iberian Peninsula, where the AR-induced precipitation pattern clearly reflected prominent east-west topographical elements, resulting in zonal bands of high and low AR impact. Over central Europe, the models simulated a smaller propagation distance of AR toward eastern Europe than obtained using the ERAI data.

Our models showed that AR in a future warmer climate will be more frequent and more intense, especially in the higher-emission scenarios (RCP4.5, RCP8.5). However, assuming low emissions (RCP2.6), the related changes can be mostly mitigated. According to the high-emission scenario RCP8.5, AR-induced precipitation will increase by 20–40% in western central Europe, whereas mean precipitation rates increase by a maximum of only 12%. Over the Iberian Peninsula, AR-induced precipitation will slightly decrease (~6%) but the decrease in the mean rate will be larger (~15%). These changes will lead to an overall increased fractional contribution of AR to heavy precipitation, with the greatest impact over Iberia (15-30%) and western France (~15%). Likewise, the fractional share of yearly maximum precipitation attributable to AR will increase over Iberia, the UK, and western France.

Over Norway, average AR precipitation rates will decline by −5 to −30%, most likely due to dynamic changes, with AR originating from latitudes >60°N decreasing by up to 20% and those originating south of 45°N increasing. This suggests that AR over Norway will follow longer routes over the continent, such that additional moisture uptake will be impeded. By contrast, AR from >60°N will take

up moisture from the North Atlantic before making landfall over Norway. The found changes in the local AR pathway are probably driven by larger scale circulation changes such as a change in dominating weather regimes and/or changes in the winter storm track over the North Atlantic.

1 Introduction

50 Atmospheric rivers (AR) are long, narrow corridors that transport enormous amounts of moisture from tropical and subtropical origins poleward (e.g., Zhu et al., 1998; Gimeno et al., 2014; Gimeno et al., 2016; Shields et al., 2019). Due to their intense moisture loads, they play an important role in the global water cycle. It has been estimated that AR are responsible for >90% of meridional moisture transport through mid-latitudes (e.g., Gimeno et al., 2016, Gimeno et al., 2018). In addition, AR are
55 associated with very powerful low-level winds often positioned at the head of a cold front of an extra-tropical storm system (e.g., Dacre et al., 2015; Gimeno et al., 2016). Accordingly, they are modulated by large-scale weather regimes, as demonstrated by Pasquier et al. (2019). In the North Atlantic sector, the moisture contained in AR originates mainly from the subtropical Atlantic (Ramos et al., 2016a). Although AR can occur throughout the year, due to their strong linkage to extra-tropical storm
60 systems they are more frequent during the cold season in the Northern Hemisphere (Lavers and Villarini 2013; Ramos et al., 2015).

In the North Atlantic and North Pacific, AR pose a serious risk of heavy precipitation and flooding along the western coasts of California and Europe (e.g., Ralph et al., 2006; Neiman et al., 2011;
65 Ralph and Dettinger, 2012; Lavers et al., 2011, Lavers et al., 2012; Lavers and Villarini; 2013; Ramos et al. 2015; Gao et al., 2016, Nayak et al., 2016; Nayak et al., 2017). Flooding is expected to increase under a warming climate, incurring high economic costs as well (Ashley et al., 2005; Sayers et al., 2015; Alfieri et al., 2016). Elucidation of the mechanisms that give rise to AR and thus to an increased flood risk is therefore essential to mitigate their impact (e.g., Kouski 2014; Alfieri et al., 2018).
70
Several studies have examined heavy precipitation events and flooding in Europe attributable to AR. For example, Lavers and Villarini (2013) analyzed atmospheric reanalysis data and found that between 1979 and 2011 as many as eight of the ten annual maximum precipitation events were related to AR. In Europe, most damage associated with AR occurs along the western continental
75 margin, especially over the Iberian Peninsula, the UK, and Scandinavia (Lavers et al. 2013, Ramos et al., 2015; Whan et al., 2020). However, AR can also penetrate far inland, producing heavy rainfall events as far east as Germany and Poland (Lavers and Villarini, 2013, Ionita et al., 2020). Unlike the heavy precipitation events associated with the local formation of short-lived convective cells during summer, AR typically produce hazardous precipitation continuously over several days (Shields and
80 Kiehl, 2016). Nonetheless, with their intense precipitation, AR also strongly contribute to local groundwater management. In dry and semi-arid regions, they can play an important role in local water groundwater recharge and the irrigation of dry land vegetation (Albano et al., 2017) as is the case in many regions around the Mediterranean (Martos-Rosillo et al., 2015).

85 Because of the larger water-holding capacity characteristic of a warmer atmosphere, climate warming is expected to increase the risk of intense flooding (e.g., Held and Soden,2006). Lavers et al. (2015) demonstrated that an intensification of the global water cycle due to climate warming will strengthen the mean transport rate of atmospheric water over the North Atlantic by 30–40%. So far, assessments of AR in a future warmer climate have been primarily based on climate projections from global models
90 (e.g., Lavers et al., 2013; Warner et al., 2015, Ramos et al., 2016; Gao et al., 2016; Espinoza et al., 2018; Whan et al., 2020). For example, Lavers et al. (2013) analyzed five global models from the Couple Model Intercomparison Project (CMIP5, Taylor et al., 2012) and found an intensification of AR in terms of their frequency and moisture load in a future climate. Based on the RCP4.5 and RCP8.5 scenarios, Ramos et al. (2016) determined a doubling of AR frequency together with an increased

95 moisture load at the end of the 21st century compared to the historical period. Gao et al. (2016) analyzed an ensemble of 24 CMIP5 global models and found a pronounced increase in the fractional contribution of AR-induced precipitation to the total annual precipitation, based on global projections following the RCP8.5 scenario. Whan et al. (2020) used the high-resolution version of the CMIP5 EC-Earth model to study the impact of climate change on AR-induced precipitation over Norway. Up to

100 80% of the winter maximum precipitation was shown to be associated with ARs. The authors also found that the magnitude of extreme precipitation events is mainly controlled by AR intensity.

The aforementioned studies analyzed global models from the CMIP5 and CMIP6 frameworks, in which the spatial resolution typically ranges from 1° to 3°. This resolution is sufficient to assess the

105 large-scale impact of climate on precipitation but it is unable to fully resolve small scale characteristics such as small convective cells (Hoheneger et al., 2020; Stevens et al., 2020). A further shortcoming of global models is their poor representation of orography, which in both CMIP5 and CMIP6 is typically lower than in the real world and thus leads to the over-simplifications of modeled processes (Baldwin et al., 2021) associated with, e.g., the uplift or blockage of an air mass. While high-resolution climate

110 models covering a limited region largely settle these issues, regional model assessments that focus on AR are still lacking for Europe. Therefore, in this study, a high-resolution regional climate model for Europe was employed to downscale global climate simulations derived from the CMIP5 suite.

The main purposes of this study are to:

115 - conduct the first analysis of AR over Europe using a downscaled CMIP5 model ensemble,
- investigate the added value of high resolution in representing AR in a climate model,
- assess future climate related changes in AR characteristics over Europe,
- explore uncertainties with respect to the choice of the global model and in regard to the choice of the greenhouse gas (GHG) emission scenario.

120
In the following, we present the first analysis of AR in a regional climate ensemble for Europe based on a horizontal resolution of 0.22°. The ensemble was used to examine future changes in AR frequency and AR-induced heavy precipitation patterns over Europe as well as the impact of AR on the local water budget. Climate-induced changes in the pathways of AR on their journey across

125 Europe were analyzed. Finally, uncertainties with respect to three different climate scenarios (RCP2.6, RCP4.5, RCP8.5) and nine different parent global climate models from the CMIP5 suite were assessed.

The paper is structured as follows: Section 2 briefly presents the regional climate model (RCA) and

130 the AR detection procedure. Section 3 describes the validation of the climate model, based on a comparison of downscaled CMIP5 historical simulations with ERAI reanalysis data. The added value of a high resolution is demonstrated by downscaling the ERAI reanalysis (Dee et al., 2011) from 0.75° resolution to 0.22° using the high-resolution model RCA. Section 4 analyzes future changes in AR frequencies and the impact on precipitation under different climate scenarios. Section 5 discusses

135 uncertainties with respect to the choice of the driving global model. Our main conclusions make up Section 6.

2. Methods

2.1. The regional climate model RCA

140 The atmospheric part of the regional climate model (Wang et al., 2015; Gröger et al., 2015; Dieterich et al., 2019) is based on Rossby Center regional atmosphere model RCA (Samuelsson et al., 2011; Kupiainen et al., 2014) version 4. RCA was set up for the Euro-Cordex domain (Fig. 1). The horizontal

resolution is 0.22° on a rotated grid, which results in a metric resolution of ~24 km (Table 1). The vertical resolution is given by 40 hybrid levels. At the lateral boundaries, the model is driven either by

145   reanalysis data (ERAI, Dee et al., 2011) or global climate model output. Hence, there is no feedback from the RCA to outside the model domain. This means that AR enter the model domain from the parent global model but then develop freely and independently of the model. The forcing data are prescribed at 6-hourly time intervals.

The land-surface boundary is defined according to ECOCLIMAP (Champeaux et al., 2005) and used

150   to calculate mass and energy fluxes between the Earth's surface and the atmosphere. Over the North Sea and Baltic Sea, RCA is interactively coupled to the 3D ocean model NEMO (Nucleus for European Modelling the Ocean NEMO, Madec, 2012, Fig. 1, Table 1). Sea ice temperature, sea ice fraction, sea ice albedo, and water temperature over this region are explicitly modeled by NEMO. Air–sea mass and energy fluxes are then calculated in the atmosphere model and used to drive NEMO,

155   which is set up at a resolution of 2 nautical miles (~3.7 km) and 56 vertical varying z^* layers. Coupling is managed by the OASIS coupler (Valcke et al., 2003). However, with its high resolution and short time stepping, NEMO is very expensive to run. Therefore, outside the coupled domain, i.e., the Mediterranean and North Atlantic, RCA is driven by reanalysis data or global climate model output.

Model system	Atmosphere component	Ocean component	Domain size Atmosphere	Domain size ocean model	Grid resolution atmosphere	Vertical levels	Temporal resolution
RCA	RCA	NEMO3.3.1	Euro-Cordex	North Sea, Baltic Sea	0.22° (~24x24 km)	40	6 hours
ERAI	IFS (Cy31r2)	Prescribed SSTs	global	global	0.75°(80x45 km)	60	6 hours

Table 1: The climate model RCA configuration employed in this study. The analyzed data set from the ERAI reanalysis is also shown (Dee et al., 2011).

160   The climate model RCA has been intensively validated and comprehensively described (e.g., Wang et al., 2015; Gröger et al., 2015; Dieterich et al., 2019; Gröger et al., 2019; Gröger et al., 2021a). It has been employed in previous studies to investigate the present climate and simulate the mean response to global climate change by downscaling global climate scenarios (Dieterich et al., 2019; Gröger et al., 2019; Gröger et al., 2021a). Gröger et al. (2021a) showed that the RCA-NEMO coupled ensemble is

165   well within the range of the high-resolution Euro-Cordex ensemble (Jacob et al., 2014). However, significant differences arise for interactively coupled areas over the sea (Gröger et al., 2021a; Gröger et al., 2021b). This applies to both climatic mean changes and climatic extremes (e.g., dry periods cold spells, heat waves).
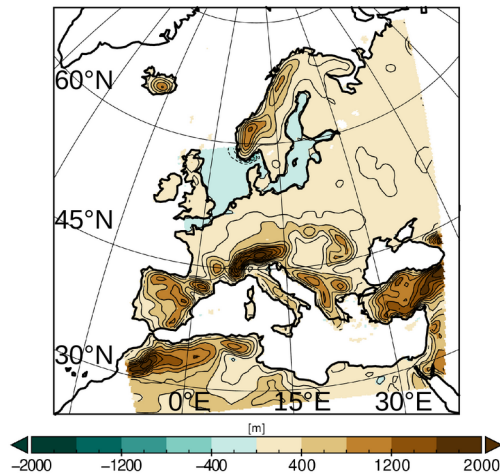
Figure 1: Model domain showing the land topography of the RCA climate model (in shades of brown). Bathymetry information is within the domain of the interactively coupled ocean model NEMO (in shades of blue).

170   **2.2 The high-resolution climate ensemble**

The above-described model was used to downscale a set of global model climate scenarios taken from the CMIP5 suite. Table 2 lists the downscaled RCA simulations as well as the applied scenarios (first row) and individual model configurations (first column).

175

Reg. mod – Glob. model	Historical (1970-1999)	RCP2.6 (1970-1999)	RCP4.5 (1970-1999)	RCP8.5 (1970-1999)
RCA – CANESM2	x		x	x
RCA – CNRM-CM5	x		x	x
RCA – EC-Earth	x	x	x	x
RCA – GFDL-ESM2M	x	x	x	x
RCA – HadGEM2-ES	x	x	x	x
RCA – IPSL-CM5A-MR	x		x	x
RCA – MIROC5	x	x	x	x
RCA – MPI-ESM-LR	x	x	x	x
RCA – NorESM1-M	x	x	x	x
Hindcast period	**(1979-2008)**			
RCA – ERAI	x			
ERAI – (ECMWF-IFS)	x			

Table 2: Overview of the 34 regional RCA simulations grouped by GHG emission scenarios and downscaled global models. For validation purposes, an RCA-ERAI hindcast was carried out for subsequent comparison with the ERAI hindcast data set. Due to technical issues, RCP2.6 scenarios for RCA – IPSL-CM5A-MR, RCA – CanESM2, and RCA – CNRM-CM5 could not be performed.

The chosen climate scenarios follow the protocol of the Representative Concentration Pathways (RCP) used in CMIP5 and derive from three different GHG emission assumptions. The low-emission scenario RCP2.6 assumes both vigorous mitigation actions (van Vuuren et al. 2007, 2011) to limit the global mean temperature increase to +2°C compared to the pre-industrial period and negative

180   emissions during the last decade of the 21st century. RCP4.5 is a moderate-emission scenario in which emissions peak at mid-century (2040) and remain constant after ~2080, at a value about half of

that at the end of the historical period (Clarke et al. 2007; Thomson et al. 2011). In the totally unmitigated scenario RCP8.5 (Riahi et al. 2007; Riahi et al., 2011), rising emissions until the end of the century are assumed. The three scenarios impose a maximum radiative forcing of 2.6, 4.5, and 8.5 W/m^2 compared to pre-industrial conditions.

In addition to the climate simulation, we produced a hindcast run with RCA forced by ERAI reanalysis data at the lateral boundaries (RCA-ERAI, Dee et al., 2011, Table 2). In this study, the hindcast was compared with the original ERAI data, which have a resolution of only 0.75° but the same temporal resolution of 6 hours (Table 1). The original ERAI data was interpolated onto the grid of the RCA climate model using the bilinear remapping technique provided by the "climate data operators" software package (Schulzweida, 2021). This comparison demonstrated the added value of downscaling. For a full description of the ERAI reanalysis data set, the reader is referred to Dee et al. (2011).

2.3 Detection of atmospheric rivers

A number of studies have addressed methods to detect AR, based on model simulations in a Eulerian framework (Lavers et al., 2011; Lavers et al., 2012; Nayak et al., 2014; Nayak and Villarini, 2016; Gao et al., 2015; O'Brian et al., 2020). An overview of some of those methods can be found in Shields et al. (2018). In our study, we employed the detection algorithm developed by Lavers et al. (2012) and Lavers and Villarini (2013), as it has been successfully applied in hindcast simulations and in future projections (Lavers and Villarini, 2012; Lavers et al., 2013). In this algorithm, vertically integrated atmospheric water vapor transport ([kg m^{-1} s^{-1}], hereafter IVT) is calculated at every 6-hourly model output time step. The vertical integration is done over pressure levels ranging from 1000 to 300 hPa (Lavers et al., 2012):

$$IVT = \sqrt{\left(\frac{1}{g}\int_{1000}^{300} qudp\right)^2 + \left(\frac{1}{g}\int_{1000}^{300} qvdp\right)^2}$$

where g is gravitational acceleration [m s^{-2}], q is specific humidity [kg/kg], u and v are horizontal wind components [m/s], and dp [Pa] is the pressure level difference of adjacent pressure levels.

Next, the detection algorithm is launched (Lavers and Villarini, 2013). It is composed of the following steps:

1. From the 6-hourly IVT time series between 1970-1999 all time steps at 12:00 UTC are extracted.

2. Along 10°W, all IVTs are sampled separately in seven meridional 5° bins between 35-70°N, i.e. 35-40°N, 40-45°N,... 65-70°N. Hence, the sample size for each meridional 5° bin consists of ~ 30 (years) * 365 (12:00 UTC) * N (number of grid cells in the respective 5°-bin at 10°W).

3. For each of the seven bins the 85th percentile IVT is calculated. The 85th percentile serves then as the threshold in the detection of AR (Lavers and Villarini 2012; Lavers and Villarini; Fig. 2).

After the bin-specific IVT thresholds were determined, the entire IVT time series containing all time
225 steps (00:00, 06:00, 12:00, 18:00) is searched for ARs.

4. AR are detected separately for each of the seven 5° latitudinal bins along 10°W and at every time
step. If the max IVT within the respective bin exceeded the threshold for that bin (Fig. 2) a search is
conducted from 10°W westward to 30°W and eastward to 25°E. All grid cells in which the threshold is
230 exceeded are retained together with its time stamps (Lavers and Villarini, 2013).

5. The resulting AR time series is then further evaluated according to spatial and temporal criteria
(Lavers and Villarini, 2013). Hence, the axis of a potential AR is determined as a maximum IVT value
along subsequent longitudes and the total length is calculated. Following Lavers and Villarini (2013)
235 and Lavers et al., 2015) in our study only those fields in which the AR axis was longer than 1500 km
were retained. Due to our limited domain, the algorithm does not detect AR that do not reach Europe
but remain out over the Atlantic Ocean. Thus, across the western Iberian Peninsula, which is located
relatively close to the model's western boundary, some AR might have been missed or detected with
a delay (as it may take longer to reach the 1500-km criterion when the AR proceeds into the model).
240 Over the UK and Norway, this did not have a significant effect as these countries lie far away from the
model's lateral boundary.

6. At this stage the retained AR fields can contain more than one AR at every time step because an
AR may cover two adjacent bins. These double entries are removed.
245

7. Finally, ARs are checked for "lifetime". ARs must have a lifetime of at least 18 hours, corresponding
to three or more consecutive 6-hourly output time steps. All other time steps were discarded.

8. During the detection, for the purpose of post-analysis, AR masks are generated and archived at a
250 resolution of 6-hourly time steps during the lifetime of the AR. The masks are based on the
exceedance of the bin thresholds along 10°W (as shown in Fig. 2) and contain information on the
moisture content as well as the date and time (Fig. 3). This allows calculation of the mean IVT within
an AR. The masks are also used to calculate the mean precipitation associated with AR and to
analyze the routes taken by the AR over the European continent.
255

Note: for the ERAI data set and the RCA-ERAI (Table 2) hindcast simulation the analysis period is
1979 – 2008, as ERAI data from before 1979 are not available.
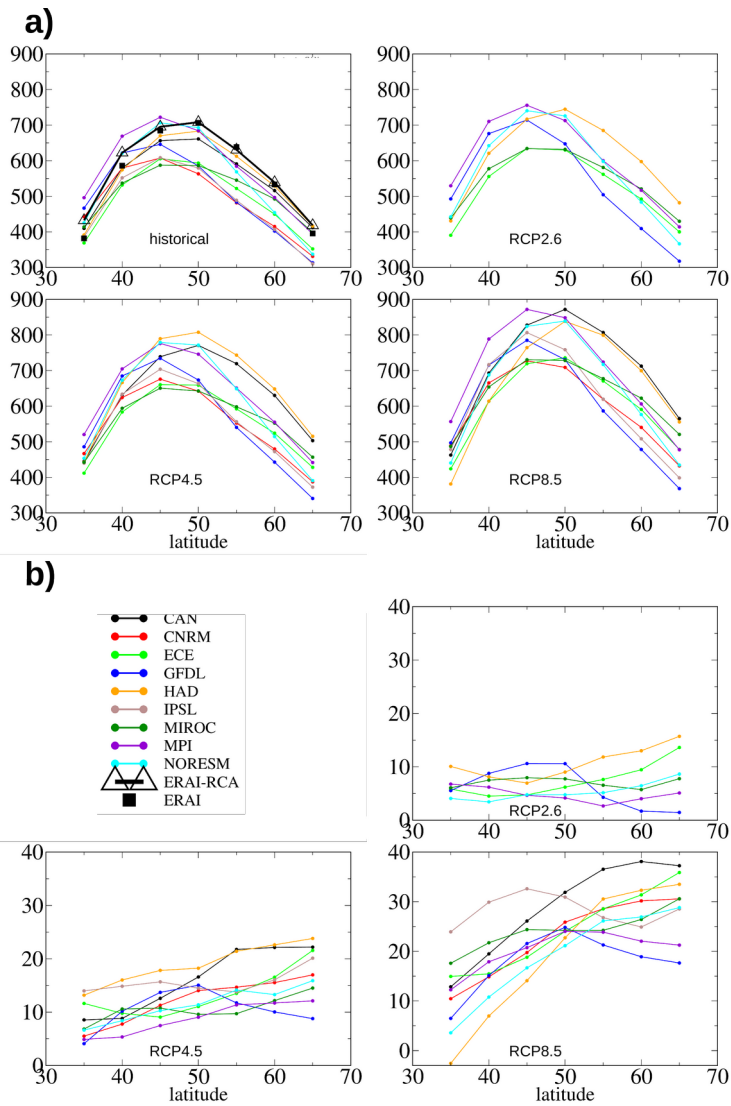
Figure 2: a) The 85th percentiles of IVT [kg m⁻¹ s⁻¹] at 10°W for all models and the historical period (1970-1999, upper left) and the RCP climate scenarios (2070-2099). The algorithm uses the values to find AR. b) Relative change [%] in the IVT thresholds in future scenarios relative to the respective historical period.

Figure 3 provides an example of an AR that caused intense rain over France and Germany and was detected in the ERAI reanalysis (left) and in the ERAI hindcast simulation (right). The detection procedure is performed separately for the historical and future periods and for each model (Table 2).
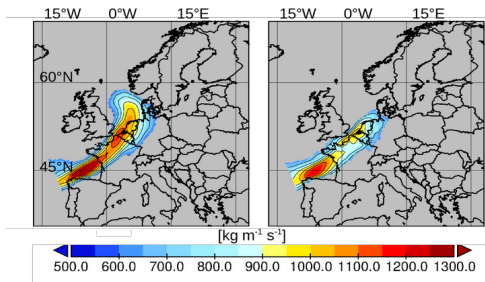
Figure 3: AR associated with storm Lothar, detected in the ERAI reanalysis (left) and in the ERAI hindcast simulation (right), 25 December, 1999; 0:00:00 UTC. IVT values below the AR 85th percentile are masked out.

2.4 Detection in future climate

Unlike previous studies (e.g., Lavers et al., 2013; Gao et al., 2016, Ramos et al., 2016), in this study we did not use the historical thresholds to detect ARs in a future climate. Instead, the IVT thresholds were calculated based on the respective climatologies between 2070 and 2099. This was done to keep the empirical relationship between the 85th percentile IVT and the moisture content in AR derived for the present climate. Hence, according to weather data for the years 1998–2005, the 85th percentile at noon (12:00) corresponded roughly to the median moisture content of the observed AR (see Lavers and Villarini., 2013 for details).

Figure 2 shows that the 85 percentile can strongly increase in the future climate depending on the scenario, the latitude, and the respective model. An example is RCA-CAN for which the IVT threshold increases by nearly 40% in RCP8.5 north of 55°N (Fig. 2b). In this simulation the 85th percentile IVT from the historical run at 55°N corresponds to the 68th percentile in the future period.

Hence, in this study a stable empirical relationship between the 85th percentile and the median was assumed. Consequently, our approach limits the influence of the larger mean atmospheric moisture content in the future climate and instead emphasizes dynamic changes.

2.5 Calculation of indices

The impact of AR under present and future climate was investigated by calculating the following indices:

1. **ARF**: The AR frequency expressed as a percent of AR days per total days within a 30-year period. A calendar day is classified as an AR day if within the 24 hours at least one AR event is recognized. Even if only one of the four 6-hourly time steps during the day is impacted by an AR, the day is counted as an AR day. Consequently, an AR lasting 18 hours and extending over two days is counted as two AR days. No distinction was made whether an AR day was associated by precipitation or not.

2. **%AMP:** The percent annual maximum precipitation rate related to AR: For every land point, the maximum precipitation rate for every year is extracted together with the date and time of its occurrence. Then every grid cell is checked to determine whether this annual maximum is related to an AR at this time and position (using the aforementioned AR masks). Hence, if 15 out of the 30

annual maxima are attributable to AR, the %AMP is equal to 50%.

3. **%95P**: The fractional contribution (%) of AR-related precipitation to the total heavy precipitation (precipitation events > 95th percentile precipitation).
1) The precipitation is summed if the associated precipitation rate exceeds the 95th percentile precipitation calculated from all precipitation events.
2) This is repeated but only for those precipitation rates related to AR. Thus, the %95P is the percent contribution of AR-related precipitation to the total heavy precipitation.

4. **%TP:** The same as the %95P but all precipitation events are considered. Thus, the %TP is the percent contribution of AR-related heavy precipitation to the total precipitation.

3. ARs in the historical simulations and hindcasts

3.1 Differences in IVT thresholds in historical, and hindcast simulations

A comparison of the latitudinal-dependent IVT thresholds of the RCA simulations with those derived from ERAI is shown in Figure 2a. As expected, the RCA-ERAI (triangles in Fig. 2a) hindcast simulation was closest to the ERAI reanalysis (filled squares). Notable discrepancies between the two data sets occurred at latitudes 40°N and 35°N. Due to the rotated grid of the RCA, the positions 35°N and 40°N at 10°W were closest to the western lateral boundary of the RCA (Fig. 1). The discrepancies most likely stem from known issues with lateral boundary coupling, as occurs in limited area models with one-way coupling to the global models (e.g., Davies, 2013; Chikhar and Gauthier 2017). Moreover, the southern model boundary at 35°N lies in the transition zone between dry air masses from the subtropics and the wet air masses of the westerlies. In this transition zone, large gradients in moisture content over short distances can be expected. Consequently, small differences in the mean position of the transition zone can cause large differences in the local moisture content.

The pronounced differences that characterize the different RCA historical simulations (Fig. 2a) reflect the different climates derived from the parent global models at the lateral boundary. First, the parent global models differ in their thermodynamic equilibrium states, such that both the air temperatures and the moisture loads at the lateral boundary of the RCA differ as well. As a result, the large-scale atmospheric circulation also differs among the global models (e.g., Brands, 2021), as the equator-to-pole temperature gradients are likewise different (Harvey et al., 2014). This further influences the meridional position of the westerlies in the respective models. For example, the maximum moisture transports are located around 50°N in RCA-HAD, RCA-CAN, and RCA-MIROC but at 45°N in the other historical runs.

There was no evidence of a linear relationship between climate warming and the increase in IVT thresholds (Fig. 2b). For example, in RCA-HAD the IVT at 35°N in the low and moderate warming scenarios (RCP2.6 and RCP4.5) increased by ~10% and ~15%, respectively (Fig. 2b). In the strongest warming scenario (RCP8.5), however, the IVT decreased by ~5%. This suggests that, over the long term, dynamic changes influence the IVT. Also decadal variations in wind components and specific humidity have to be considered in this context (Thandlam et al., 2021).

3.2 General statistics

Table 3 summarizes the number of AR for each run of the climate ensemble and the ERAI reanalysis

340 data set and for the RCA-ERAI hindcast run. The results were almost identical for the RCA-ERAI hindcast (322) and ERAI reanalysis itself (321), which was used to drive the RCA. This indicates that the number of AR in the RCA is primarily controlled by the parent global model at the lateral boundaries. This is not surprising since AR develop in open ocean regions far outside the model's domain. However, within that domain the RCA develops freely, leaving its own fingerprint on AR, by

345 controlling their intensity, geometry, and lifetime (Fig. 3). The RCA fingerprint is likely to become stronger with growing distance from the lateral boundaries. Analogously, AR in the respective RCA climate simulations (Table 3) will reflect the AR generated from the driving global climate model. Consequently, the RCA historical climate ensemble had a fairly large spread during the historical period, ranging from 262 (RCA-MIROC) to 421 (RCA-NORESM). The difference between the

350 ensemble mean (RCA-MEAN) of the historical simulations (RCA-MEAN=359) and the RCA-ERAI hindcast run (n=322) was small compared to the standard deviation over the RCA historical ensemble (58).

Compared to the historical period, RCA-MIROC increased by 15% in RCP 4.5 but only by 5% in the

355 strongest warming scenario (RCP8.5, Table 3) which is lowest increase in the ensemble. Hence, there was no linear scaling with global mean warming compared to the other models. This can be explained by the changes in the large-scale circulation in the parent global model, such as induced by shifts in the eddy-driven jet (Gao et al., 2016).

	Historical/ Hindcast	RCP26	RCP45	RCP85
RCA-ERAI	322			
ERAI reanalysis	321			
RCA climate ensemble				
RCA-MEAN	359	390.0 (+8.6)	425.7 (+18.6)	445.6 (+24.1)
RCA-STD	58	67.4 (+16.46)	71.50 (+23.6)	90.3 (+56.0)
RCA-CAN	367		445 (+21.3)	447 (+21.8)
RCA-CNRM	285		317 (+11.2)	362 (+27.0)
RCA-ECE	393	396 (+0.76)	412 (+4.8)	468 (+19.1)
RCA-GFDL	351	367 (+4.6)	388 (+10.5)	456 (+29.9)
RCA-HAD	397	422 (+11.3)	484 (+21.9)	565 (+42.3)
RCA-IPSL	409		498 (+21.8)	523 (+27.9)
RCA-MPI	304	311 (+2.3)	350 (+15.1)	392 (+29.0)
RCA-MIROC	262	264 (+0.76)	302 (+15.3)	276 (+5.3)
RCA-NORESM	421	417 (-0.91)	457 (+8.6)	521 (+23.8)

Table 3: Number of AR detected in a 30 year period of different climate scenarios. The historical period for all runs is 1970-1999. The exception is the ERAI run, for which it was 1979–2008. Numbers in parenthesis denote the relative change (%) in the future vs. the historical period.

A comparison of the moisture transported by AR over land is shown in Figure 4a, which depicts the

360   potential of AR to force local heavy precipitation events. Note that the moisture content over land is lower in the RCA-ERAI run than in the ERAI (~5%, Fig. 4a). This is in line with the model's cold bias in air temperature (Gröger et al., 2021a), thus favoring a lower moisture content. The lower moisture content in RCA-MEAN than in the RCA-ERAI hindcast simulation should also be pointed out. Overall, this suggests a systematic negative bias in the moisture content over land in the RCA model. The

365   distribution of diagnosed AR durations (Fig. 4b) does not indicate systematic differences between the ERAI reanalysis, the hindcast run, and the mean historical climate simulations. For all model realizations, about half of the detected AR lasted one day or less (Fig. 4b)
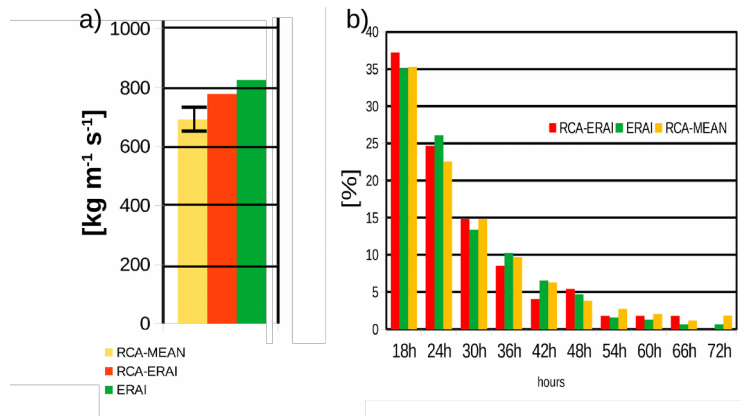
Figure 4: a) Average AR moisture transport over land for each model realization depicted from the climatological historical period (RCA-MEAN) as well as for the hindcast simulation (RCA-ERAI) and the reanlysis data set (ERAI). For RCA-MEAN the range of two standard deviations from individual model simulation is given. b) Histogram of average durations of detected AR.

370   **3.3 Impact on precipitation**

Maps of AR frequencies (ARF) over land are presented in Figure 5a. As expected, during the historical period AR were most abundant over the UK and the coastal regions of western Europe. Further inland, AR frequencies declined as the AR lost moisture due to rainfall and thus no longer met the IVT threshold. Strong moisture losses also occurred along the Norwegian coast, where AR

375   landfalls caused heavy rain events due to orographic uplift.

We then evaluated the potential of AR to cause annual maxima of daily precipitation (Fig. 5b, %AMP). Locally, AR explained up to ~60% of the yearly maxima over southwestern Norway. A strong imprint was likewise seen over the western UK and along European coasts, where AR were responsible for

380   up to 50% of the annual maxima in RCA-MEAN and RCA-ERAI.
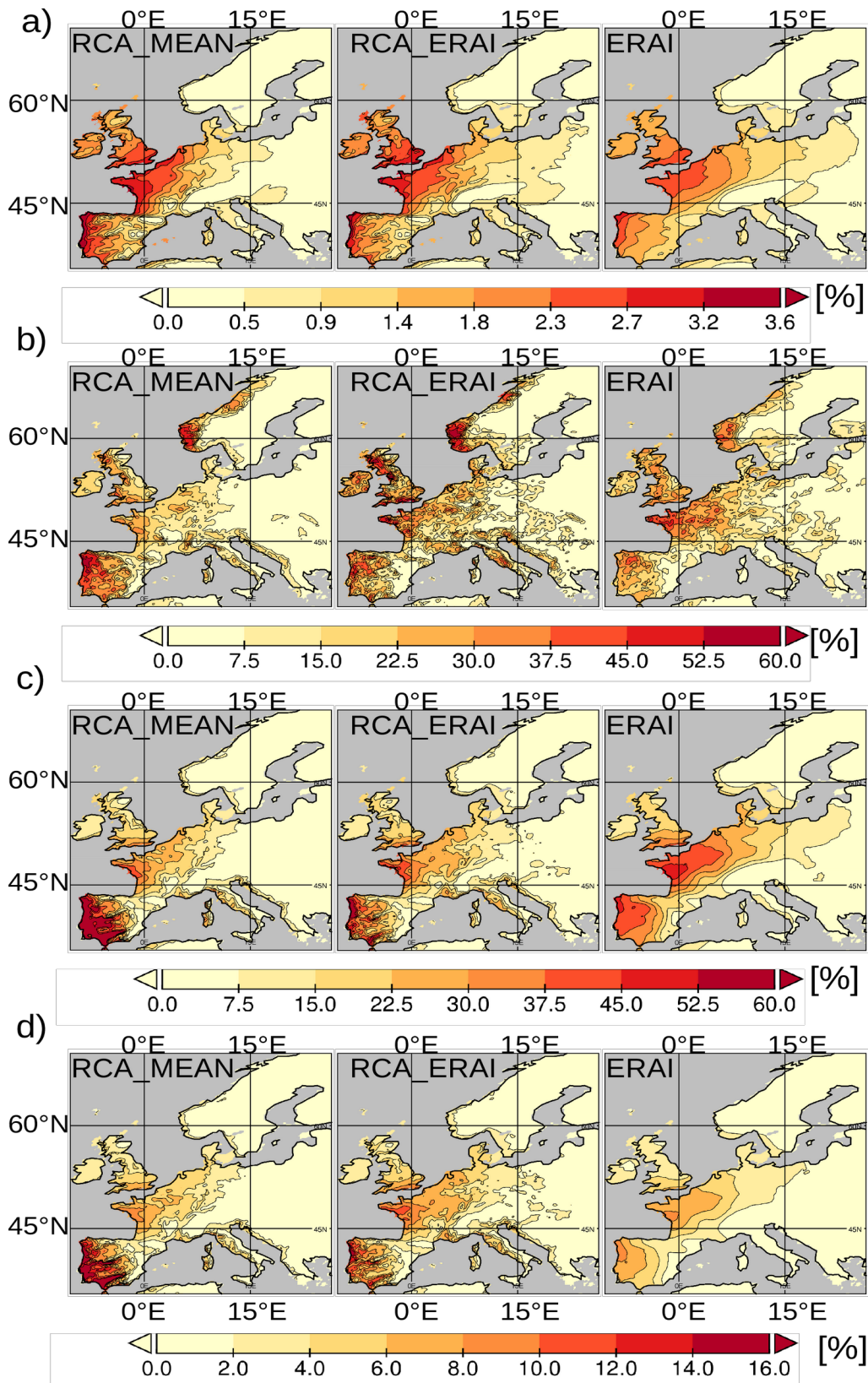
Figure 5: AR frequency expressed as the total number of days a grid cell was covered by an AR during the historical period (ARF). b) Percentage of the annual maximum precipitation related to AR (%AMP). c) Fractional contribution of AR-forced precipitation to the >95th percentile precipitation (%95P). d) Same as c) but for the total precipitation (%TP).

Besides their potential to cause yearly precipitation maxima, AR give rise to heavy precipitation
385 events. The fractional contributions of AR to heavy precipitation (%95P) and to the total
precipitation (%TP) are shown in Figure 5c and 5d. The spatial pattern mainly mirrored the AR
frequency pattern but it also reflected the varying long-term mean hydrological conditions in
Europe: In semi-arid regions such as the Iberian Peninsula and along the western coast of Italy,
%95P increased to almost 60% and 30%, respectively. Under the humid climate of central and
390 western Europe, the %95P was smaller but it reached 40% in western France and the southern UK
(Fig. 5c). In the mountainous regions of Norway and in the Alps, i.e., regions with very high mean
precipitation and frequent convective rain events, the influence of sporadic AR was accordingly
low. A similar pattern characterized the fractional contribution to the total annual precipitation
(%TP, Fig. 5d). Maxima occurred over western France and the western Iberian Peninsula, where
395 AR accounted for up to 10% of the total precipitation.

3.4 Effect of Downscaling

The effect of downscaling was assessed by comparing the 0.75° ERAI reanalysis (Fig. 5, right
400 column) with the 0.22° RCA-ERAI hindcast simulation (Fig. 5 middle column). The lower resolution
of ERAI eliminated much of the spatial variability, thus highlighting the effect of the downscaling by
RCA. This was most visible in the noisy precipitation-related indices %AMP, %95P, and %TP (Fig.
5b–d). This was expected because spatial precipitation patterns are modulated by stochastic
processes associated with, e.g., small convection cells and further affected by topography. The
405 representation of convection cells and topography has been shown to benefit from a higher
resolution (e.g., Feser et al., 2011; Hoheneger et al., 2020; Stevens et al., 2020). The pronounced
effect of a higher topographic resolution was seen over the Iberian Peninsula. Here, RCA-ERAI
clearly resolved the distinct effect of the prominent west–east topographic features seen in the
fractional contributions to the precipitation budget. Those features appeared as small distinct
410 WSW-ENE bands of alternating high and low %95P and a %TP that followed the topographic
elements built up by the Sistema Central Plateau, the Sierra Morena mountains, and the Penibaetic
orogenic system (Fig. 5c,d, and middle columns). By contrast, in ERAI (Fig. 5c,d, right column)
there was a simple decline of the %95P while the %TP occurred at a longer distance from the
coast and did not reflect any topographic imprint. For the Iberian Peninsula, added value of
415 regional downscaling was previously reported for the simulation of mean precipitation and mean
temperature patterns (Gomez-Navarro et al., 2011).

Another noteworthy difference was the considerably larger number of AR-related annual maxima
(%AMP, Fig. 5b) over Norway, West Scotland, and Italy in RCA-ERAI than in ERAI. In the latter,
420 the AR influence on %95P and %TP was much more extensive in eastern Europe. However, there
are no major topographical elevations in eastern Europe, which suggests that resolution is not the
only factor accounting for this difference. Rather, differences in the model's physics (e.g. cloud
formation) and the surface boundary conditions (e.g., surface temperature, surface roughness
parametrization) between RCA-ERAI and ERAI could influence the extent of AR penetration into
425 eastern Europe.

Finally, we note that the comparison between different spatial resolutions might also reflect
430   different noise levels. This noise occurs when isolated grid points located outside the AR at a given time step exceed the IVT threshold but do not satisfy the geometric and temporal requirements. The different noise levels would then contribute to the total effect of downscaling.

3.5 Comparison of the RCA ensemble mean with the ERAI hindcast and ERAI reanalysis

435

Global climate models can have considerable biases on a regional scale. Consequently, when driven by global climate models at the boundaries, RCA will not perform as well as hindcast models when the driving lateral boundaries are constrained to reanalysis data. Therefore, in the following, before assessing climate change scenarios, we briefly compare the results of the RCA historical
440   ensemble mean (RCA-MEAN, Fig. 5, left column) with the RCA-ERAI hindcast (Fig. 5, middle column) and ERAI reanalysis data (Fig. 5, righ column).

For ARF, %AMP, %95P, and %TP, RCA-MEAN reasonably well reproduced the spatial pattern obtained with the RCA-ERAI simulation. The spatial correlation coefficients between RCA-ERAI
445   and RCA-MEAN were 0.98 for ARF (Fig. 5a), 0.86 for %AMP (Fig. 5b), 0.82 for %TP (Fig. 5c), and 0.92 for %95P (Fig. 5d). Similar to RCA-ERAI, the imprint over eastern Europe was distinctly weaker according to RCA-MEAN than according to the ERAI data set.

Pronounced differences between RCA-MEAN and RCA-ERAI also occur over the Iberian
450   Peninsula, where the values of %AMP, %95P, and %TP are systematically higher in RCA-MEAN. Overall, the best match between RCA-MEAN and RCA-ERAI is for the parameter ARF (Fig 5a). As ARF is calculated only from the IVT, it is less effected by biases in precipitation. Thus, the main contributor to the biases of RCA-MEAN seen in %AMP, %95P, and %TP are attributable to the simulated precipitation, not to the IVT. We note that the exact reproduction of precipitation pattern
455   is difficult in coarse resolution models due to insufficient description in cloud physics and/or the treatment of convective energy (e.g Prein et al., 2013; Hohenegger et al., 2020).

The detected AR were also characterized by a strong seasonal cycle that was well reproduced by RCA-MEAN. Figure 6 shows that AR were most abundant during fall and early winter. The only notable difference was in August, when the relative share was about twice as large in the RCA
460   historical ensemble than in the ERAI hindcast. In addition, RCA-MEAN and RCA-ERAI highly overestimate the number of AR in September compared to ERAI but underestimate it in October. However, overall, AR were better represented in the model's climate mode (RCA-MEAN) than in the RCA-ERAI hindcast simulation.

465
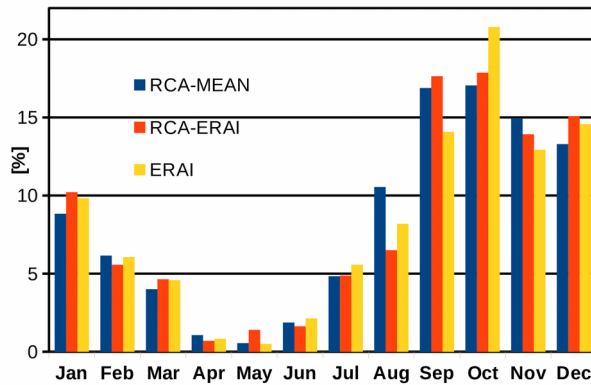
Figure 6: Seasonal cycle of detected AR at 10°W, expressed as the percent share of the total number of detected AR. The reference period for the RCA historical ensemble (RCA-MEAN, blue) was 1970–1999 and for the ERAI hindcast (orange) and ERAI (yellow) reanalysis 1979–2008.

4. Future climate change impact on ARs

4.1 General response of AR frequency and intensity

The relative change in average moisture transported by AR for each of the GHG emission
470   scenarios and each of the downscaled global models is summarized in Figure 7. AR became
consistently more intense, i.e., they had a higher moisture load, in a warmer climate. The average
intensity at the end of the century indicated by RCA-MEAN increased by 6% (RCP2.6), 13%
(RCP4.5), and 24% (RCP8.5). These values are generally in line with the corresponding increases
in the IVT thresholds (Fig. 2b).

475

The number of detected AR also increased (Table 3). For RCA-MEAN, this number increased by
9%; 19%, and 24% in RCP2.6, RCP4.5, and RCP8.5, respectively. These values were roughly
proportional to the increase in intensity. However, not only the frequency of AR but also the spread
of the individual realizations at the end of the century increased. The relative change in the
480   ensemble spread (Table 3, 2nd row) increased even more than the ensemble average
(RCP2.6=17%, RCP4.5=24%, RCP8.5=56%). This highlighted the large uncertainty with respect to
the chosen global model used for downscaling. Advanced approaches for weighted model
averaging have been developed to reduce this type of uncertainty and have been tested for AR
occurring over the US (Massoud et al., 2019; Massoud et al., 2020, Wootten et al., 2020).

485
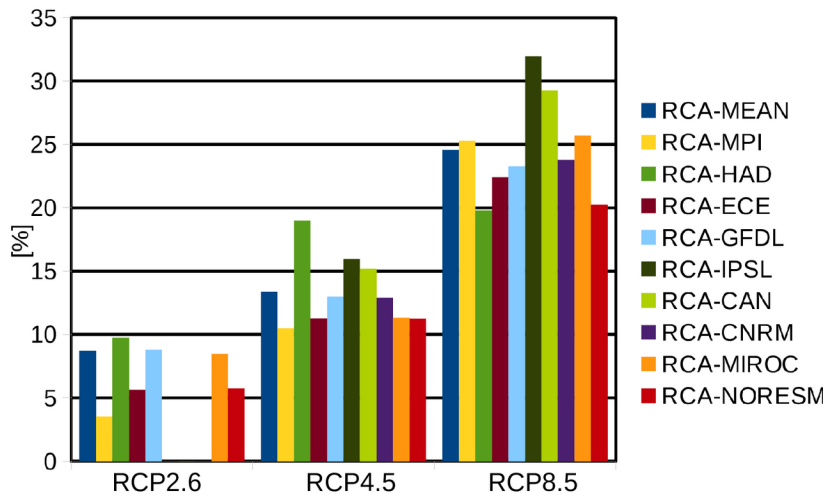
Figure 7: Relative change in moisture transport within AR at the end of the century (2070-2099) compared to the historical period (1970-1999). RCA-MEAN denotes the mean of the individual models. Note no RCP2.6 realizations are available for RCA-IPSL, RCA-CAN, and RCA-CNRM.

4.2 Spatial changes

The change in the spatial patterns is shown in Fig. 8. An overall increase in AR day frequency was
490   determined for scenarios RCP4.5 and RCP8.5 (Fig. 8a). The strongest increase occurred near the
Bay of Biscay and adjacent land areas (western France and southern UK). This response over land
was more or less consistent across the RCP scenarios but differed in strength, ranging from
~+0.2% to > +1.8% in RCP4.5 and RCP8.5 (Fig. 8a). This corresponds to a relative increase of 20–
120% (RCP4.5) or 40–250% (RCP8.5) over Iberia, the UK, France Germany, and along the
495   Norwegian coast.

Figure 8b shows the changes in the yearly maximum precipitation attributed to AR (%AMP). The
most robust change was the strong increase over the western central part of Europe, extending
from western France along the coast of Belgium, the Netherlands, northern Germany, and
500   Denmark up to the southern coast of Norway. Further sites of stronger AR impact were also visible
along the northwestern area of the Iberian Peninsula and the southern UK whereas over southern
Scandinavia there were no robust changes. However, in this area %AMP was already very high
during the historical period (Fig. 5b), which limited the potential for further increases. This increase
over the UK, France, western Germany, and Iberia was by far the strongest in the unmitigated
505   RCP8.5 scenario. In the moderate scenario RCP4.5, the changes were less pronounced in eastern
central Europe (Germany, Denmark). In the mitigation scenario RCP2.6, robust changes were
restricted to a small area in NW France (Brittany, Normandy).
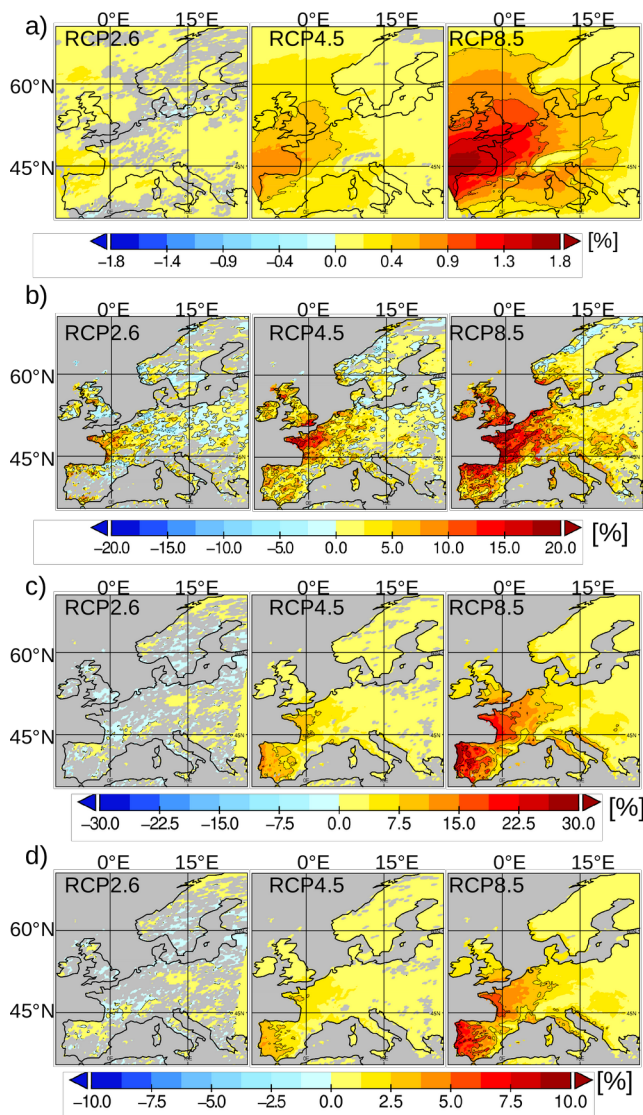
Figure 8: Difference between 2070-2099 minus 1970-1999 (i.e. the % values for the future minus the % values for the historical). a) AR days frequency (ARF), b) AR forced yearly maximum precipitation rates (%AMP). c) Change in the AR fractionial contribution to the heavy precipitation (%95P). d) same as c) but for the fraction to the annual total precipitation (%TP). Note that all non-robust changes (at least 66% of downscaled runs agree on the sign of change) have been masked out. Shown are ensemble mean differences.

The higher AR frequencies and moisture loads also had consequences for local precipitation budgets. The fractional contributions of AR to the heavy precipitation fraction (%95P, Fig. 8c) and to the total annual precipitation (%TP, Fig. 8d) increased nearly everywhere for RCP4.5, and RCP8.5. The most pronounced changes were in regions where the %95P and %TP were already large under historical conditions (Fig. 5c,d). In RCP8.5, the strongest increases primarily occurred in western Iberia and along the French coast (Bay of Biscay), where heavy rain precipitation increased by up to +30% and up to 20%, respectively, compared to the historical period.

The elevated AR fractional contributions %95P and %TP in RCP4.5 and RCP8.5 (Fig. 8c,d) suggested that in these scenarios the increase in the AR induced precipitation rates was higher than the increase in the average precipitation rates.

The relative changes in mean precipitation and AR-induced precipitation for RCP8.5 are compared in Fig. 9. The mean precipitation change (Fig. 9a) was consistent with the typically dryer conditions over southern Europe and the typically wetter conditions over northern Europe (e.g. Jacobs et al., 2014;

525 Kjellström et al., 2018; Teichmann et al., 2018; Gröger et al., 2021a; Christensen et al., 2021). Hence, mean precipitation rates increased only slightly, by at most 12%, over central Europe or even decreased over southern Europe. By contrast, AR-induced precipitation increased ~25–40% over central Europe (Fig. 9b). Decreasing AR precipitation also occurred in southern Europe but the reductions were weaker than the reductions in the mean rates. The exception was Norway, where

530 AR-induced precipitation decreased while the mean rates increased. The lower AR precipitation rates well agree with the low response in western Norway of the %AMP, which locally even decreased (Fig. 8b).
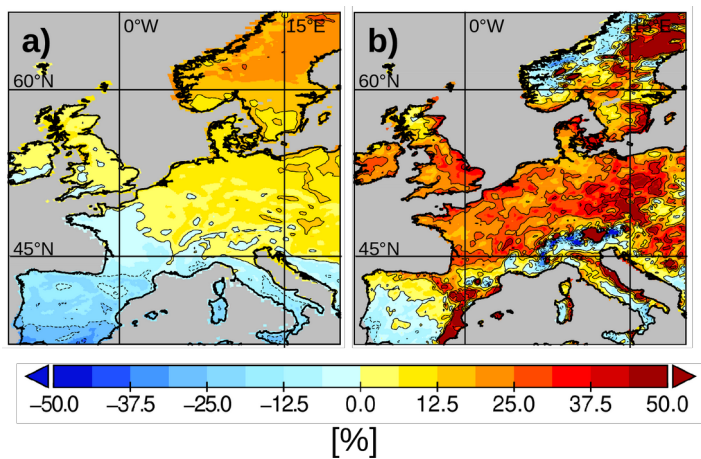
Figure 9: Relative change (difference between 2070-2099 and 1970-1999) in a) the average precipitation rates and b) the AR induced precipitation rates for RCP8.5. Shown are ensemble mean differences.

535 **4.3 Influence of dynamical changes**

The dynamic changes were investigated by exploring the route followed by AR east of the 10°W meridian. In this analysis, AR masks were used (see Fig. 3) and, for the model's land grid cells the corresponding latitudinal position where the AR crosses the 10°W meridian was determined. All land grid cells overlain by the respective AR were then flagged with the latitudinal bin at 10°W (for

540 example, 45°N for the bin 45-50°N). The flagged masks were then used to calculate, for every land cell, the percent share for every latitudinal bin (with the sum of all bins at every land point defined as 100%). This was done for the periods 1970–1999 and 2070–2099. Then, the future change (difference between 2070–2099 and 1970–1999) was calculated for RCP8.5. Finally, the latitudinal bins were consolidated into three main meridional bands: south of 45°N, 45-60°N, and north of 60°N.

545

Our analysis showed not only the more frequent occurrence of AR in the future at all latitudes but also a change in their composition (with respect to the meridional band where they originate). AR contributions from >60°N declined everywhere (Fig. 10a), with a ~20% reduction over Norway, but also over many European mountainous regions, such as the Pyrenees, Massif Central, Alps,

550 mountains in the Balkans (Fig. 10a). The smaller fraction was paralleled by a relative increase in AR

originating from south of 45°N (Fig. 10c) while the fraction from 45°–60°N was more or less unchanged (Fig. 10b).

The larger fraction of more southern ARs over Norway (and the smaller fraction from >60°N) has two implications: 1) the more southern AR will carry warmer air masses to Scandinavia, such that precipitation will tend to fall more often as rain than as snow. 2) Moisture transport via southern AR implies that the moisture is routed over longer distances across the central continent before it arrives in Norway. AR traversing the continent can no longer take up significant amounts of moisture but instead lose moisture via precipitation. By contrast, AR originating from >60°N and crossing the open North Atlantic can take up moisture until they make landfall at the Norwegian coast. This is in particular the case during the warm season when SST are high enough to allow convection or during winter when moisture convergence advects moisture from adjacent areas. These changes likely account for the lower AR precipitation rates determined along the western coast of Norway (Fig. 9b).

5 Discussion

5.1 Uncertainties with respect to the choice of CMIP5 models

Climate models are designed and validated to simulate the mean state and mean variability of the long-term climate. Hence, the validation of climatic extremes during model development is relatively small. As a result, the models results will differ more for extreme regimes. Figure 11 shows the inter-model standard deviations for the different percentiles of precipitation. The percentiles were calculated for all nine models (Table 2) covering the historical period. For the higher percentiles, the spread over the models clearly increases, such that uncertainties are highest in the extreme precipitation range, i.e., the range where AR precipitation is expected to occur. Therefore, to assess the uncertainties associated with model choice, in the following we consider the spread in the ensemble members with respect to ARF, %AMP, and 95P%.
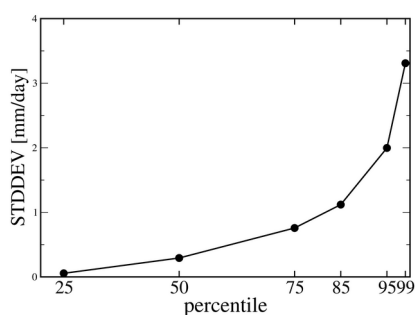
Figure 10: Inter-model standard deviation from the nine downscaled models calculated for the 25th, 50th, 75th, 85th, 95th, 99th percentiles of precipitation. The average over all the land grid cells of the models is shown. The percentiles have been derived from the 6-hourly time-series of precipitation.

Figure 12a depicts the frequency of AR days. All realizations exhibited a coherent spatial pattern that
580   was similar to the RCA ensemble mean (Fig. 8a), indicating the latter as a representative indicator of
the bulk response. The uncertainties in the model spread as indicated by the ensemble's standard
deviation (Fig. 12a) were highest in the southern UK, France, Belgium, the Netherlands, Luxembourg,
and western Iberia. In conclusion, the uncertainty in the response is highest in those regions where
AR are frequent already during the historical period (Fig. 5a). RCA-HAD, RCA-CAN, RCA-IPSL and
585   RCA-GFDL showed the strongest response, whereas the response in RCA-MIROC and RCA-ECE
was exceptionally weak. The weak climate impact in RCA-MIROC is a direct consequence of low
increase in detected AR (~5%, Table 3). Only one single model shows a clear signal along the
Norwegian coast (RCA-HAD) and whole Scandinavia.

590   The response of AR-forced annual maximum precipitation events (%AMP) is shown in Figure 12b. No
clear consistent response was detected over western Norway, i.e., the region where in the historical
climate the %AMP was highest (Fig. 5b). Some models (RCA-CAN, RCA-MPI, RCA-GFDL, RCA-
IPSL) showed distinct locations over Norway where the impact of AR was smaller in the future,
probably linked to the aforementioned decrease in AR arising from >60°N. The most coherent change
595   across the realizations was the relatively strong increase over western France, which in some
realizations extended further east. However, also in this region the local ensemble variability was
pronounced and in RCA-ECE the %AMP in fact decreased.

Uncertainties with respect to the contribution to heavy precipitation (%95P) were highest in France
600   and Iberia (Fig. 12c). High inter-model variation was determined also for the southern tip of Iberia,
where the standard deviation was highest. In this region, the contribution of AR was either reduced,
as in RCA-HAD, or increased by as much as 50%, as in RCA-CNRM. Larger uncertainties were
likewise identified for central Europe (France, Belgium, Netherlands, Germany), with the direction of
change being consistently positive. In RCA-HAD, RCA-CNRM, RCA-ECE, and RCA-MIROC, the
605   changes over eastern France and Germany were extremely low. A notable decrease, occurring in the
UK was modeled only by RCA-HAD.
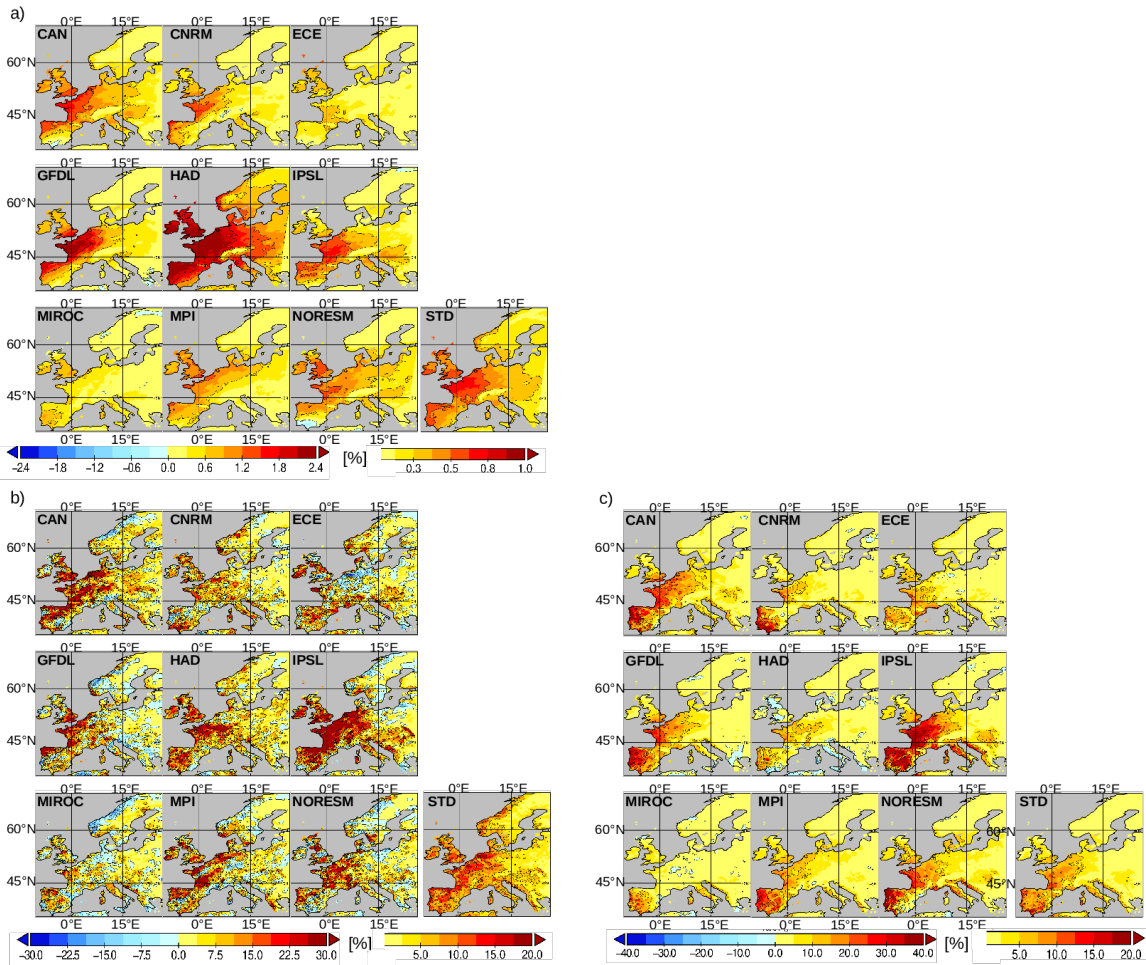
Figure 11: Change in AR day frequency (2070-2099 minus 1970-1999). b) same as a) but for percentage in AR forced yearly maximum precipitation (%AMP), c) same as a) but for AR fractional contribution to heavy precipitation (%95P). Note the RCA realization are denoted by their forcing global model simply. STD denotes the inter-model standard deviation across all 9 models (CAN, CNRM,...NORESM). Long bars indicate the color scale of the ensemble member indices. Short bars are for inter-model standard deviation. All maps reflect changes for RCP8.5.

In summary, our analysis showed a robust inter-model agreement for the general spatial pattern.

610 However, local uncertainty is high especially in %AMP (i.e. the most severe precipitation events, Fig. 12b), where even the direction of change is not consistent.

5.2 Differences to global projections

Our results generally agree with those of the global CMIP5 models (e.g., Lavers et al., 2013; Gao et

615 al., 2016; Ramos et al., 2016), with both indicating more frequent and more intense AR over Europe. With respect to previous studies, the effect of climate change on AR frequency has been shown to strongly depend on the chosen reference period. Studies that applied the 85th percentile threshold derived from the historical period also to the future period often reported a doubling of the AR frequency (e.g., Lavers et al., 2013, Ramos et al., 2016; Gao et al., 2016). However, as noted above

620 we calculated separate 85th percentile thresholds for these two periods, and the AR frequency increase was therefore lower (because the IVT thresholds for the future period were higher; Fig. 2) than that in the aforementioned studies but nonetheless 20–30% across the models.

625 The main differences with respect to global projections occurred over Norway and the Iberian Peninsula, two hotspots of AR impact in Europe. Over Iberia, the distribution of AR-related heavy precipitation was clearly modulated by topographic structures, including the Sistema Central Plateau, the Sierra Morena mountains, and the Penibaetic orogenic system. These valleys and ridges will lead to zonal bands of high and low increases in AR precipitation over Iberia in the future. Over Norway,
630 our regional ensemble did not predict a robust climate change signal for the frequency of ARF, %AMP, %95P, or %TP (Fig. 8). Global CMIP5 models indicated an increase in the regional %TP and %95P of at least 10–20% according to RCP8.5 (Gao et al.,2016, Fig. 9 therein). In our regional model, %AMP was either negative or positive, depending on the global model, and thus did not yield a clear signal (Fig. 12b).

635

Our finding that in a future high-emission scenario AR from south of 45°N will be more common over Europe than AR from >60°N points to larger-scale atmospheric circulation in the parent global models. While such changes cannot be analyzed in our limited area model, it can be proposed that they are related to changes in the storm track (Zappa et al., 2013) and/or systematic changes in regional
640 weather systems (Pasquier et al., 2018).

6. Summary and Conclusions

A high-resolution regional climate model ensemble with a resolution of 0.22° was created to investigate the impact of AR in Europe. The added value of downscaling was demonstrated by a
645 hindcast that was run to downscale the ERAI reanalysis data set with a resolution of 0.75°. In the central and southern Iberian Peninsula, the contribution of AR to the regional precipitation budget was shown to be strongly affected by prominent topographic signatures. This feature was not seen in the ERAI reanalysis data, which instead showed distinct E-W gradients in which precipitation was highest in the west. The AR imprint on the analyzed indices in the ERAI data set was weak over Iberia but
650 stronger in distant parts of Eastern Europe compared to the downscaled RCA-ERAI (Fig. 5).

The regional climate model was further used to investigate AR in present and future climates. Thus, an ensemble of global CMIP5 climate simulations (1.4°–3° resolution) was downscaled to reach a 0.22° resolution. In total, 34 simulations were carried out for the GHG emission scenarios RCP2.6,
655 RCP4.5, and RCP8.5.

The historical simulations from the regional climate model ensemble were in good agreement with the global ERAI reanalysis data set and the ERAI simulation hindcast run. In the regional climate ensemble, AR had the strongest impact in near-coastal regions, explaining up to 60% of the yearly
660 maximum precipitation rates in regions with orographic uplift (e.g., Norway). Over Iberia and western France, the fractional contribution of AR to total precipitation (%TP) and heavy precipitation (%95P) was up to 20%, and >40%, respectively.

Our results showed that in a future warmer climate AR become more frequent and carry a larger
665 moisture load, consistent with the findings of previous studies (e.g., Lavers et al., 2013; Warner et al., 2015; Gao et al., 2016; Shields and Kiehl, 2016; Ramos et al., 2016; Shields et al., 2016; Shields et

al., 2019; Massoud et al., 2019; Whan et al., 2020). The potential of ARs to force annual maximum precipitation events is likely to be highest over western France (Brittany) and northernmost Spain, by up to 20% (RCP8.5), whereas no robust ensemble response was determined over Norway. Our

670 regional high-resolution model thus allows a spatially more accurate calculation of the fractional contributions of AR to the local water budget than is possible with global earth system models. It showed that, in the future, the increase in AR-induced precipitation will be larger than the increase in average precipitation such that the fractional contributions of AR to heavy rain (%95P) and total rain (%TP) will also be larger, increasing by up to 10%, and 30%, respectively.

675

Our study also showed that AR day frequencies over Europe will increase over all latitudes along the 10°W meridian, albeit with a larger increase at southern than at northern latitudes. This leads to a higher fractional contribution of AR over Europe from more southern latitudes, which in turn affects the route that AR follow east of 10°W. Since the moisture then travels a longer distance over land, a

680 further uptake of moisture by the AR before it arrives in Norway is prevented. For RCP8.5, this should lead to locally decreased precipitation rates over western Norway. By contrast, during the historical period, a larger share of AR came from >60°N, arriving in Norway directly from the North Atlantic.

Elsewhere in Europe, our study clearly demonstrated that, under the higher GHG emission scenarios

685 RCP4.5 and RCP8.5, a larger imprint of AR on the regional scale and a larger role of heavy precipitation forcing events with a potential risk for flooding can be expected. However, under RCP2.6, most of the climate-induced changes are not robust and may thus be responsive to climate mitigation actions.

690 Our regional assessment of the impact of AR on Europe must be considered as a first step, since the realized horizontal resolution is still relatively coarse (24 km) and does not explicitly resolve convection. The next generation of regional high-resolution models will improve the resolution to only a few kilometers and allow to resolve convection (e.g. Giorgi, 2019; Jacob et al., 2020). These advances will allow a more thorough investigation of the processes mediating the response of AR to

695 climate change and the pathways of AR across Europe.

Acknowledgements
The research presented in this study is part of the Baltic Earth program (Earth System Science for the Baltic Sea region, see http://www.baltic.earth). Regional climate scenario simulations have been

700 conducted on the Linux clusters Krypton, Bi, Triolith and Tetralith, all operated by the National Supercomputer Centre in Sweden (http://www.nsc.liu.se/). Resources on Triolith and Tetralith were funded by the Swedish National Infrastructure for Computing (SNIC) (grants SNIC 002/12-25, SNIC 2018/3-280 and SNIC 2019/3-356). The Swedish Civil Contingencies Agency (MSB) and the Swedish Research Council for Sustainable Development (FORMAS) have contributed funding through the

705 HydroHazards project (MSB 2019-0651). Additional funding was obtained by the Swedish Research Council for sustainable development (Formas) through the ClimeMarine project, funded within the framework of the National Research Programme for Climate (grant no. 2017-01949). Finally we thank 3 anonymous reviewers for a thorough reading of the manuscript and excellent recommendations that helped to improve the article.

710

Data availability declaration

The datasets generated during and/or analyzed during the current study are available from the corresponding author on reasonable request.

715 **Competing interests**

The authors declare that they have no conflict of interest.

Code/data availability

Numerical model codes available from the respective literature and corresponding first author. Data to reproduce results presented in this study are available upon reasonable request.

720

References

Albano, C. M., M. D. Dettinger, and C. E. Soulard: Influence of atmospheric rivers on vegetation productivity and fire patterns in the southwestern US. J. Geophys. Res. Biogeosci., 122, 308–323, https://doi.org/10.1002/2016JG003608, 2017

725

Alfieri, L., Dottori, F., Betts, R., Salamon, P., Feyen, L. (2018), Multi-Model Projections of River Flood Risk in Europe under Global Warming. *Climate*, *6*, 6, doi:10.3390/cli6010006.

Alfieri, L., Bisselink, B., Dottori, F., Naumann, G., de Roo, A., Salamon, P., Wyser, K. and Feyen, L.
730 (2017), Global projections of river flood risk in a warmer world. Earth's Future, 5: 171-182. https://doi.org/10.1002/2016EF000485

Ashley, .R. M., Balmforth, D.J., Saul, A.J., and Blanskby, J.D. (2005), Flooding in the future – predicting climate change, risks and responses in urban areas. *Water Sci Technol* 1, 52 (5): 265–273.
735 doi: https://doi.org/10.2166/wst.2005.0142

Baldwin, J. W., Atwood, A. R., Vecchi, G. A., & Battisti, D. S. (2021). Outsize influence of Central American orography on global climate. *AGU Advances*, 2, e2020AV000343. https://doi.org/10.1029/2020AV000343
740

Brands, S.: A circulation-based performance atlas of the CMIP5 and 6 models for regional climate studies in the northern hemisphere, Geosci. Model Dev. Discuss. [preprint], https://doi.org/10.5194/gmd-2020-418, in review, 2021

745 Cabos, W., de la Vara, A., Álvarez-García, F.J. *et al.* Impact of ocean-atmosphere coupling on regional climate: the Iberian Peninsula case. *Clim Dyn* **54,** 4441–4467 (2020). https://doi.org/10.1007/s00382-020-05238-x

Champeaux, J.L., Masson, V. and Chauvin, F. (2005), ECOCLIMAP: a global database of land
750 surface parameters at 1 km resolution. Met. Apps, 12: 29-32. https://doi.org/10.1017/S1350482705001519

Clarke L, Edmonds J, Jacoby H, Pitcher H, Reilly J, Richels R (2007) Scenarios of greenhouse gas emissions and atmospheric concentrations. Sub-report 2.1A of Synthesis and Assessment Product
755 2.1 by the U.S. Climate Change Science Program and the Subcommittee on Global Change Research. Department of Energy, Office of Biological & Environmental Research, Washington, 7 DC., USA, pp 154

760 Chikhar, K., & Gauthier, P. (2017). Impact of Lateral Boundary Conditions on Regional Analyses, *Monthly Weather Review*, *145*(4), 1361-1379.

Christensen, O.B., Kjellström, E., Dieterich, C., Gröger, M., Meier, H.E.M. (2021). Regional climate projections for the Baltic Sea Region until 2100, Earth System Dynamics, accepted.

765 Dacre, H. F., P. A. Clark, O. Martinez-Alvarado, M. A. Stringer, and D. A. Lavers (2015), How do atmospher ic rivers form?, Bull. Am. Meteorol. Soc., 96(8), 1243–1255, http://dx.doi.org/10.1175/BAMS-D-14-00031.1

Davies, T. (2014), Lateral boundary conditions for limited area models. Q.J.R. Meteorol. Soc., 140:
770 185-196. https://doi.org/10.1002/qj.2127

Dee, D.P., Uppala, S.M., Simmons, A.J., Berrisford, P., Poli, P., Kobayashi, S., Andrae, U., Balmaseda, M.A., Balsamo, G., Bauer, P., Bechtold, P., Beljaars, A.C.M., van de Berg, L., Bidlot, J., Bormann, N., Delsol, C., Dragani, R., Fuentes, M., Geer, A.J., Haimberger, L., Healy, S.B., Hersbach,
775 H., Hólm, E.V., Isaksen, L., Kållberg, P., Köhler, M., Matricardi, M., McNally, A.P., Monge-Sanz, B.M., Morcrette, J.-J., Park, B.-K., Peubey, C., de Rosnay, P., Tavolato, C., Thépaut, J.-N. and Vitart, F., The ERA-Interim reanalysis: configuration and performance of the data assimilation system. Q.J.R. Meteorol. Soc., 137: 553-597. https://doi.org/10.1002/qj.828, 2011

780 Dettinger, M. D. (2011), Climate change, atmospheric rivers, and floods in California—A multimodel analysis of storm frequency and magnitude changes. Journal of the American Water Resources Association, 47(3), 514–523

Dettinger MD. 2013. Atmospheric rivers as drought busters on the U.S. West Coast. *J. Hydrometeor.*
785 14:1721–32, https://doi.org/10.1175/JHM-D-13-02.1

Dieterich, C., Wang, S., Schimanke, S., Gröger, M., Klein, B., Hordoir, R., Samuelsson, P., Liu, Y., Axell, L., Höglund, A., Meier, H.E.M. (2019a): Surface heat budget over the North Sea in climate change simulations. Atmosphere, 10, 272. doi:10.3390/atmos10050272.
790
Dieterich, C. and Gröger, M. and Arneborg, L. and Andersson, H. C., 2019b. Extreme sea levels in the Baltic Sea under climate change scenarios -- Part 1: Model validation and sensitivity, Ocean Sci, 15, 6, 1399-1418, 10.5194/os-15-1399-2019

795 Di Luca, A., de Elía, R. & Laprise, R. Potential for added value in precipitation simulated by high-resolution nested Regional Climate Models and observations. *Clim Dyn* **38,** 1229–1247 (2012). https://doi.org/10.1007/s00382-011-1068-3

Espinoza, V., Waliser, D. E., Guan, B., Lavers, D. A., & Ralph, F. M. (2018). Global analysis of climate
800 change projection effects on atmospheric rivers. Geophysical Research Letters, 45, 4299–4308. https://doi.org/10.1029/2017GL076968

Emori, S., and Brown, S. J. (2005), Dynamic and thermodynamic changes in mean and extreme precipitation under changed climate, *Geophys. Res. Lett.*, 32, L17706, doi:10.1029/2005GL023272
805
Feser F. , Rockel B. , von Storch H. , Winterfeldt J. , Zahn R . Regional climate models add value to global model data: a review and selected examples. Bull. Am. Meteorol. Soc. 2011; 92(9): 1181–

1192. DOI: 10.1175/2011BAMS3061.1

810 Gao, Y., Lu, J., & Leung, L. R., Uncertainties in Projecting Future Changes in Atmospheric Rivers and Their Impacts on Heavy Precipitation over Europe, *Journal of Climate*, *29*(18), 6711-6726; DOI: https://doi.org/10.1175/JCLI-D-16-0088.1, 2016.

Gimeno L, Nieto R, Vázquez M and Lavers DA (2014) Atmospheric rivers: a mini-review. *Front. Earth*
815 *Sci*. **2**:2. doi: 10.3389/feart.2014.00002

Gimeno, L., Dominguez, F., Nieo, R., Trigo, R., Drumond, A., Reason, C. J.C., Taschetto, A.S., Ramos, A.M., Kumar, R., Marengo, J., (2016), Major Mechanisms of Atmospheric Moisture Transport and Their Role in Extreme Precipitation Events, Annual Review of Environment and
820 Resources 2016 41:1, 117-141

Giorgi F (2019) Thirty years of regional climate modeling: Where are we and where are we going next? J Geophys Res 124:5696–5723. https://doi.org/10.1029/2018JD030094

825 Gómez-Navarro, J. J., Montávez, J. P., Jerez, S., Jiménez-Guerrero, P., Lorente-Plazas, R., González-Rouco, J. F., and Zorita, E.: A regional climate simulation over the Iberian Peninsula for the last millennium, Clim. Past, 7, 451–472, https://doi.org/10.5194/cp-7-451-2011, 2011.

Gröger, M., Dieterich, C., Meier, H.E.M., Schimanke, S., (2015) Thermal air–sea coupling in
830 hindcast simulations for the North Sea and Baltic Sea on the NW European shelf, Tellus A: Dynamic Meteorology and Oceanography, 67:1, DOI: 10.3402/tellusa.v67.26911

Gröger, M., Arneborg, L., Dieterich, C., Höglund, A., and Meier, H.E.M. (2019), Summer hydrographic changes in the Baltic Sea, Kattegat and Skagerrak projected in an ensemble of climate scenarios
835 downscaled with a coupled regional ocean–sea ice–atmosphere model. Clim Dyn 53, 5945–5966 doi:10.1007/s00382-019-04908-9

Gröger, M., Dieterich, C., Meier, H.E.M., (2021a), Is interactive air sea coupling relevant for simulating the future climate of Europe?, Climate Dynamics, doi: 10.1007/s00382-020-05489-8, 2021a.
840
Gröger, M., Dieterich, C., Haapala, J., Ho-Hagemann, H. T. M., Hagemann, S., Jakacki, J., May, W., Meier, H. E. M., Miller, P. A., Rutgersson, A., and Wu, L.: Coupled regional Earth system modeling in the Baltic Sea region, Earth Syst. Dynam., 12, 939–973, https://doi.org/10.5194/esd-12-939-2021, 2021b.
845
Hagemann, S., and L. Dümenil (1998), A parameterization of the lateral waterflow for the global scale, Clim. Dyn., 14, 17– 31

Hagemann, S., H. Göttel, D. Jacob, P. Lorenz, and E. Roeckner, Improved regional scale processes
850 reflected in projected hydrological changes over large European catchments, Clim. Dyn., 32(6), 767– 781, doi:10.1007/s00382-008-0403-9, 2009.

Harvey, B.J., Shaffrey, L.C. & Woollings, T.J. Equator-to-pole temperature differences and the extra-tropical storm track responses of the CMIP5 climate models. *Clim Dyn* **43,** 1171–1182. https://doi.org/
855 10.1007/s00382-013-1883-9, 2014.

Harvey, B. J., Cook, P., Shaffrey, L. C., & Schiemann, R. . The response of the northern hemisphere

storm tracks and jet streams to climate change in the CMIP3, CMIP5, and CMIP6 climate models. Journal of Geophysical Research: Atmospheres, 125, e2020JD032701. https://doi.org/10.1029/2020JD032701, 2020.

Held IM, Soden BJ (2006) Robust responses of the hydrological cycle to global warming. J Clim 19(21):5686–5699, https://doi.org/10.1175/JCLI3990.1.

Hohenegger, C., L. Kornblueh, D. Klocke, T. Becker, G. Cioni, J. F. Engels, U. Schulzweida, and B. Stevens, 2020: Climate statistics in gobal simulations of the atmosphere, from 80 to 2.5 km grid spacing. J. Meteor. Soc. Japan, 98, 73-91.

Ho-Hagemann, H.T.M., Gröger, M., Rockel, B., Zahn, M., Geyer, B., Meier, H.E.M. (2017): Effects of air-sea coupling over the North Sea and the Baltic Sea on simulated summer precipitation over Central Europe. Climate Dyn., pp. 1–26. doi:10.1007/s00382-017-3546-8.

Huang, X., Swain, D.L., and Hall, A.D., 2020, Future precipitation increase from very high resolution ensemble downscaling of extreme atmospheric river storms in California, Science, 6, (29), doi: 10.1126/sciadv.aba1323

Ionita, M., Nagavciuc, V., and Guan, B.: Rivers in the sky, flooding on the ground: the role of atmospheric rivers in inland flooding in central Europe, Hydrol. Earth Syst. Sci., 24, 5125–5147, https://doi.org/10.5194/hess-24-5125-2020, 2020

Jacob, D. (2001), A note to the simulation of the annual and interannual variability of the water budget over the Baltic Sea drainage basin, Meteorol. Atmos. Phys., 77(1–4), 61– 73

Jacob, D., Petersen, J., Eggert, B. *et al.* EURO-CORDEX (2014): new high-resolution climate change projections for European impact research. *Reg Environ Change* **14,** 563–578. https://doi.org/10.1007/s10113-013-0499-2

Jacob D, Teichmann C, Sobolowski S et al (2020) Regional climate downscaling over Europe: perspectives from the EURO-CORDEX community. Reg Environ Change. https://doi.org/10.1007/s10113-020-01606-9.

Jeworrek J, Wu L, Dieterich C, Rutgersson A (2017) Characteristics of convective snow bands along the Swedish east coast. Earth Syst Dyn 8:163–175. https://doi.org/10.5194/esd-8-163-2017

Jungclaus, J. H., N. Fischer, H. Haak, K. Lohmann, J. Marotzke, D. Matei, U. Mikolajewicz, D. Notz, and J. S. von Storch (2013), Characteristics of the ocean simulations in MPIOM, the ocean component of the MPI-Earth system model, J. Adv. Model. Earth Syst., 5, 422– 446, doi:10.1002/jame.20023

Kaiser-Weiss, A.K., Borsche, M., Niermann, D., Kaspar, F., Lussana, C., Isotta, F.A., van den Besselaar, E., van der Schrier, G., and Unden, P., (2019), Added value of regional reanalyses for climatological applications, Environ. Res. Commun. https://doi.org/10.1088/2515-7620/ab2ec3

Kelemen, F.D., Primo, C., Feldmann, H., Ahrens, B. (2019), Added Value of Atmosphere-Ocean

Coupling in a Century-Long Regional Climate Simulation, Atmosphere, *10*(9), 537, https://doi.org/10.3390/atmos10090537.

Kjellström, E., Nikulin, G., Strandberg, G., Christensen, O. B., Jacob, D., Keuler, K., Lenderink, G., van Meijgaard, E., Schär, C., Somot, S., Sørland, S. L., Teichmann, C., and Vautard, R. (2018), European climate change at global mean temperature increases of 1.5 and 2 °C above pre-industrial conditions as simulated by the EURO-CORDEX regional climate models, Earth Syst. Dyn., 9, 459–478, https://doi.org/10.5194/esd-9-459-2018.

Kousky C (2014) Informing climate adaptation: a review of the economic costs of natural disasters. Energy Econ 46:576–592, https://doi.org/10.1016/j.eneco.2013.09.029.

Kupiainen M. , Jansson C. , Samuelsson P. , Jones C. , Willén U. , co-authors . Rossby Centre regional atmospheric model, RCA4, Rossby Center News Letter. 2014. Online at: http://www.smhi.se/en/Research/Research-departments/climate-research-rossby-centre2-552/1.16562 .

Lavers, D. A., R. P. Allan, E. F. Wood, G. Villarini, D. J. Brayshaw, and A. J. Wade, Winter floods in Britain are connected to atmospheric rivers, Geophys. Res. Lett., 38, L23803, doi:10.1029/2011GL049783, 2011

Lavers, D. A., G. Villarini, R. P. Allan, E. F. Wood, and A. J. Wade, The detection of atmospheric rivers inatmospheric reanalyses and their links to British winter floods and the large-scale climatic circulation, J. Geophys. Res., 117,D20106, doi:10.1029/2012JD018027, 2012

Lavers, D. A., and Villarini, G. , The nexus between atmospheric rivers and extreme precipitation across Europe, *Geophys. Res. Lett.*, 40, 3259– 3264, doi:10.1002/grl.50636, 2013

Lavers, D. A. & Villarini, The contribution of atmospheric rivers to precipitation in Europe and the United States. J. Hydrol. 522, 382–390, 2015

Lavers, D. A., Allan, R.P., Villarini, G., Lloyd-Hughes, B., Brayshaw, D.J., Wade, A.J., Future changes in atmospheric rivers and their implications for winter flooding in Britain, *Environ. Res. Lett.* **8,** 034010, DOI: 10.1088/1748-9326/8/3/034010, 2013

Lavers, D. A., R. P. Allan, E. F. Wood, G. Villarini, D. J. Brayshaw, and A. J. Wade (2011), Winter floods in Britain are connected to atmospheric rivers, Geophys. Res. Lett., 38, L23803, doi:10.1029/2011GL049783.

Lavers, D. A., Ralph, F. M., Waliser, D. E., Gershunov, A., and Dettinger, M. D. (2015), Climate change intensification of horizontal water vapor transport in CMIP5, *Geophys. Res. Lett.*, 42, 5617–5625, doi:10.1002/2015GL064672

Madec G, The NEMO Team (2012) "NEMO ocean engine": Note du Pole de modélisation de l'Institut Pierre-Simon Laplace, France, No 27, ISSN no 1288-1619

Marsland, S. J., H. Haak, J. H. Jungclaus, M. Latif, and F. Roeske (2002), The Max-Planck-Institute global ocean/sea ice model with orthogonal curvilinear coordinates, *Ocean Modell.*, 5(2), 91– 126

Martos-Rosillo, S., González-Ramón, A., Jiménez-Gavilán, P. *et al.* Review on groundwater recharge

955   in carbonate aquifers from SW Mediterranean (Betic Cordillera, S Spain). *Environ Earth Sci* **74,** 7571–7581. https://doi.org/10.1007/s12665-015-4673-3, 2015.

Massoud, E. C., H., Lee, P. B., Gibson, P., Loikith, and D. E., Waliser: Bayesian Model Averaging of Climate Model Projections Constrained by Precipitation Observations over the Contiguous United

960   States, Journal of Hydrometeorology, 21, 2401-2418. https://doi.org/10.1175/JHM-D-19-0258.1, 2020.

Massoud, E. C., Espinoza, V., Guan, B., & Waliser, D. E. (2019). Global Climate Model Ensemble Approaches for Future Projections of Atmospheric Rivers. *Earth's Future*, 7: 1136– 11511151. https://doi.org/10.1029/2019EF001249

965

Nayak, M. A., and Villarini, G. (2017), A long-term perspective of the hydroclimatological impacts of atmospheric rivers over the central United States, *Water Resour. Res.*, 53, 1144– 1166, doi:10.1002/2016WR019033

970   Nayak, M. A., G. Villarini, and A. A. Bradley (2016), Atmospheric rivers and rainfall during NASA's Iowa Flood Studies (IFloodS) Campaign, *J. Hydrometeorol.*, 17(1), 257– 271

Nayak, M. A., G. Villarini, and D. A. Lavers (2014), On the skill of numerical weather prediction models to forecast atmospheric rivers over the central United States, *Geophys. Res. Lett.*, 41, 4354–

975   4362, doi:10.1002/2014GL060299

Neiman, P. J., , F. M. Ralph, , G. A. Wick, , J. D. Lundquist, , and M. D. Dettinger, 2008: Meteorological characteristics and overland precipitation impacts of atmospheric rivers affecting the west coast of North America based on eight years of SSM/I satellite observations. *J. Hydrometeor.*, **9**,

980   22–47, doi:10.1175/2007JHM855.1.

Neiman, P. J., L. J. Schick, F. M. Ralph, M. Hughes, and G. A. Wick (2011), Flooding in Western Washington: The connection to atmospheric rivers, J. Hydrometeorol., 12(6), 1337–1358

985   O'Brien, T. A., Payne, A. E., Shields, C. A., Rutz, J., Brands, S., Castellano, C., Chen, J., Cleveland, W., DeFlorio, M. J., Goldenson, N., Gorodetskaya, I. V., Díaz, H. I., Kashinath, K., Kawzenuk, B., Kim, S., Krinitskiy, M., Lora, J. M., McClenny, B., Michaelis, A., O'Brien, J. P., Patricola, C. M., Ramos, A. M., Shearer, E. J., Tung, W., Ullrich, P. A., Wehner, M. F., Yang, K., Zhang, R., Zhang, Z., & Zhou, Y. (2020). Detection Uncertainty Matters for Understanding Atmospheric Rivers, *Bulletin of the American*

990   *Meteorological Society*, *101*(6), E790-E796

Pasquier, J. T., Pfahl, S., & Grams, C. M. (2019). Modulation of atmospheric river occurrence and associated precipitation extremes in the North Atlantic Region by European weather regimes. *Geophysical Research Letters*, 46, 1014– 1023. https://doi.org/10.1029/2018GL081194

995

Payne, A.E., Demory, ME., Leung, L.R., Ramos, A.M., Shields,C.A., Rutz,J.J., Siler, N., Villarini, G., Hall, A., Ralph F.M.:, Responses and impacts of atmospheric rivers to climate change. *Nat Rev Earth Environ* **1,** 143–157, https://doi.org/10.1038/s43017-020-0030-5, 2020.

1000   Prein AF, Gobiet A, Suklitsch M, Truhetz H, Awan NK, Keuler K, Georgievski G.: Added value of convection permitting seasonal simulations. Clim Dyn 41:2655–2677. https://doi.org/10.1007/s00382-013-1744-6, 2013.

Primo, C., Kelemen, F. D., Feldmann, H., Ahrens, B. (2019): A regional atmosphere-ocean climate

1005   system model (CCLMv5.0clm7-NEMOv3.3-NEMOv3.6) over Europe including three marginal seas: on
        its stability and performance, Geoscientific Model Development Discussions, 2019, 1-33, doi:
        10.5194/gmd-2019-73

        Ralph, F. M., P. J. Neiman, G. A. Wick, S. I. Gutman, M. D. Dettinger, D. R. Cayan, and A. B. White
1010   (2006), Flooding on California's Russian River: Role of atmospheric rivers, Geophys. Res. Lett., 33,
        L13801, doi:10.1029/2006GL026689.

        Ralph FM, Dettinger MD. 2011. Storms, floods, and the science of atmospheric rivers. *EOS*
        92(32):265–66
1015
        Ralph, F. M., and M. D. Dettinger (2012), Historical and national perspectives on extreme West Coast
        precipitation associated with atmospheric rivers during December 2010, Bull. Am. Meteorol. Soc., 93,
        783–790, doi:10.1175/BAMS-D-11-00188.1.

1020   Ramos AM, Trigo RM, Liberato MLR, Tomé R. 2015a Daily precipitation extreme events in the Iberian
        Peninsula and its association with atmospheric rivers. *J. Hydrometeor.* 16:579–97

        Ramos, A. M., Nieto, R., Tomé, R., Gimeno, L., Trigo, R. M., Liberato, M. L. R., and Lavers, D. A :
        Atmospheric rivers moisture sources from a Lagrangian perspective, Earth Syst. Dynam., 7, 371–384,
1025   https://doi.org/10.5194/esd-7-371-2016, 2016a

        Ramos, A. M., R. Tomé, R. M. Trigo, M. L. R. Liberato, and J. G. Pinto (2016), Projected changes in
        atmospheric rivers affecting Europe in CMIP5 models, Geophys. Res. Lett., 43, 9315–9323,
        doi:10.1002/2016GL070634
1030
        Riahi K, Gruebler A, Nakicenovic N (2007) Scenarios of long-term socio-economic and environmental
        development under climate stabilization. Technol Forecast Soc Chang 74(7):887–935

        Riahi K, Rao S, Krey V et al (2011) RCP 8.5—a scenario of comparatively high greenhouse gas
1035   emissions. Clim Change 109:33. https://doi.org/10.1007/s10584-011-0149-y

        Samuelsson P, Jones CG, Willen U, Ullerstig A, Golvig S, Hansson U, Jansson C, Kjellström E,
        Nikulin G, Wyser K (2011) The Rossby Centre Regional Climate model RCA3: model description and
        performance. Tellus A 63:4–23. https://doi.org/10.1111/j.1600-0870.2010.00478.x
1040
        Sayers, P.B; Horritt, M; Penning-Rowsell, E; McKenzie, A. (2015) Climate Change Risk Assessment
        2017: Projections of future flood risk in the UK. Research undertaken by Sayers and Partners on
        behalf of the Committee on Climate Change. Published by Committee on Climate Change, London.

1045   Schulzweida, U.: CDO User Guide (Version 2.0.0). Zenodo. http://doi.org/10.5281/zenodo.5614769,
        2021.

        Shields, C. A., and Kiehl, J. T. (2016), Simulating the Pineapple Express in the half degree
        Community Climate System Model, CCSM4, *Geophys. Res. Lett.*, 43, 7767– 7773,
1050   doi:10.1002/2016GL069476

        Schiemann, R., Vidale, P. L., Shaffrey, L. C., Johnson, S. J., Roberts, M. J., Demory, M.-E.,
        Mizielinski, M. S., and Strachan, J. (2018): Mean and extreme precipitation over European river
        basins better simulated in a 25 km AGCM, Hydrol. Earth Syst. Sci., 22, 3933–3950,

1055   https://doi.org/10.5194/hess-22-3933-2018.

Sein, D. V., Mikolajewicz, U., Gröger, M., Fast, I., Cabos, W., Pinto, J. G., et al. (2015). Regionally coupled atmosphere-ocean-sea ice-marine biogeochemistry model ROM: 1. description and validation. J. Adv. Model. Earth Syst. 7, 268–304. doi: 10.1002/2014ms000357

1060   Sein, D.V, Gröger, M., Cabos, W., Alvarez, F., Hagemann, S., de la Vara, A., Pinto, J.G., Izquierdo, A., Koldunov, N.V., Dvornikov, A. Y., Limareva, N., Martinez, B., Jacob, D. (2020), Regionally coupled atmosphere - ocean - marine biogeochemistry model ROM: 2. Studying the climate change signal in the North Atlantic and Europe J. Adv. Model. Earth Syst., https://doi.org/10.1029/2019MS001646.

1065   Sodemann, H. & Stohl, A. (2013), Moisture origin and meridional transport in atmospheric rivers and their association with multiple cyclones. *Mon. Weather Rev.* **141**, 2850–2868

Soto-Navarro, J., Jordá, G., Amores, A. et al. Evolution of Mediterranean Sea water properties under climate change scenarios in the Med-CORDEX ensemble. Clim Dyn 54, 2135–2165 (2020).
1070   https://doi.org/10.1007/s00382-019-05105-4

Shields, C. A., and Kiehl, J. T. (2016), Atmospheric river landfall-latitude changes in future climate simulations, *Geophys. Res. Lett.*, 43, 8775– 8782, doi:10.1002/2016GL070470, 2016.

1075   Shields, C. A., Rutz, J. J., Leung, L.-Y., Ralph, F. M., Wehner, M., Kawzenuk, B., Lora, J. M., McClenny, E., Osborne, T., Payne, A. E., Ullrich, P., Gershunov, A., Goldenson, N., Guan, B., Qian, Y., Ramos, A. M., Sarangi, C., Sellars, S., Gorodetskaya, I., Kashinath, K., Kurlin, V., Mahoney, K., Muszynski, G., Pierce, R., Subramanian, A. C., Tome, R., Waliser, D., Walton, D., Wick, G., Wilson, A., Lavers, D., Prabhat, Collow, A., Krishnan, H., Magnusdottir, G., and Nguyen, P.: Atmospheric
1080   River Tracking Method Intercomparison Project (ARTMIP): project goals and experimental design, Geosci. Model Dev., 11, 2455–2474, https://doi.org/10.5194/gmd-11-2455-2018, 2018.

Shields, C. A., Rosenbloom, N., Bates, S., Hannay, C., Hu, A., Payne, A. E., et al. Meridional heat transport during atmospheric rivers in high-resolution CESM climate projections. *Geophysical*
1085   *Research Letters*, 46, 14702– 14712. https://doi.org/10.1029/2019GL085565, 2019

Stevens, B., and Coauthors, The added value of large-eddy and storm-resolving models for simulating clouds and precipitation. *J. Meteor. Soc. Japan, 98, 395–435, https://doi.org/10.2151/jmsj.2020-021, 2020*
1090

Taylor, K.E., Stouffer, R.J., and Meehl, G.A.: An overview of CMIP5 and the experiment design. Bull Am Meteorol Soc 93:485–498, 2012

Thandlam, V., Rutgersson, A. & Sahlee, E. Spatio-temporal variability of atmospheric rivers and
1095   associated atmospheric parameters in the Euro-Atlantic region. *Theor Appl Climatol* **147,** 13–33 (2022). https://doi.org/10.1007/s00704-021-03776-w.

Teichmann C, Bülow K, Otto J, Pfeifer S, Rechid D, Sieck K, Jacob D (2018) Avoiding extremes: benefits of staying below +1.5 °C compared to +2.0 °C and +3.0 °C global warming. Atmosphere
1100   9:115. https://doi.org/10.3390/atmos9040115

Valcke, S., A. Caubel, D. Declat, and L. Terray (2003), OASIS3 Ocean Atmosphere Sea Ice Soil User's Guide, Tech. Rep. TR/CMGC/03-69, CERFACS, Toulouse, France

1105   Vancoppenolle, M., Fichefet, T., Goosse, H., Bouillon, S., Madec, G., and Morales Maqueda, M. A. (2008): Simulating the mass balance and salinity of Arctic and Antarctic sea ice. 1. Model description and validation, Ocean Modell., 27, 33–53, doi:10.1016/j.ocemod.2008.10.005.

  van Haren, R., Haarsma, R. J., van Oldenborgh, G. J. & Hazeleger, W. Resolution dependence of
1110   European precipitation in a state-of-the-art atmospheric general circulation model (2015), J. Clim. 28, 5134–5149.

  van Vuuren D, den Elzen M, Lucas P, Eickhout B, Strengers B, van Ruijven B, Wonink S, van Houdt R (2007) Stabilizing greenhouse gas concentrations at low levels: an assessment of reduction
1115   strategies and costs. Clim Change. https://doi.org/10.1007/s/10584-006-9172-9

  van Vuuren DP, Stehfest E, den Elzen MGJ et al (2011) RCP2.6: exploring the possibility to keep global mean temperature increase below 2 °C. Clim Change 109:95. https://doi.org/10.1007/s10584-011-0152-3
1120
  Wang S., Dieterich C., Döscher R., Höglund A., Hordoir R., Meier HEM, Samuelsson P., Schimanke S., (2015) Development and evaluation of a new regional coupled atmosphere–ocean model in the North Sea and Baltic Sea. Tellus A 67:1. https://doi.org/10.3402/tellusa.v67.24284

1125   Wang X, Li J, Sun C, Liu T (2017) NAO and its relationship with the Northern Hemisphere mean surface temperature in CMIP5 simulations. J Geophys Res Atmos 122:4202–4227. https://doi.org/10.1002/2016JD025979

  Warner, M. D., C. F. Mass, and E. P. Salathe (2015), Changes in winter atmospheric rivers along the
1130   North American west coast in CMIP5 climate models, J. Hydrol. Meteorol., doi: 10.1175/JHM-D-14-0080.1

  Whan, K., Sillmann, J., Schaller, N. *et al.* Future changes in atmospheric rivers and extreme precipitation in Norway. *Clim Dyn* **54,** 2071–2084 (2020). https://doi.org/10.1007/s00382-019-05099-z
1135
  Wootten AM, Massoud EC, Sengupta A, Waliser DE, Lee H. The Effect of Statistical Downscaling on the Weighting of Multi-Model Ensembles of Precipitation. *Climate*. 2020; 8(12):138. https://doi.org/10.3390/cli8120138

1140   Zappa G, Shaffrey LC, Hodges KI (2013) The ability of CMIP5 models to simulate North Atlantic extratropical cyclones. J Clim 26(15):5379–5396

  Zhu, Y., and Newell, R. (1998). A proposed algorithm for moisture fluxes from atmospheric rivers. *Mon. Wea. Rev*. 126, 725–735. doi: 10.1175/1520-0493(1998)126%3C0725:APAFMF%3E2.0.CO;2
1145
  Zhu, S., Remedio, A.R.C., Sein, D.V. et al. Added value of the regionally coupled model ROM in the East Asian summer monsoon modeling. Theor Appl Climatol 140, 375–387 (2020). https://doi.org/10.1007/s00704-020-03093-8.

1150